Ferritic and martensitic ODS steel resistance upset welding of fuel claddings: Weldability assessment and metallurgical effects

Olivier Doyen, Brendan Le Gloannec, Alexis Deschamps, Frédéric De Geuser, Cédric Pouvreau, Angeline Poulon-Quintin

Ferritic and martensitic ODS steel resistance upset welding of fuel claddings: weldability assessment and metallurgical effects

Olivier DOYEN[a], Brendan LE GLOANNEC[a,d], Alexis DESCHAMPS[b], Frédéric DE GEUSER[b], Cédric POUVREAU[c], Angéline POULON-QUINTIN[d].

a Den-Service d'études mécaniques et thermiques (SEMT), CEA, Université Paris-Saclay, F-91191 Gif-sur-Yvette, France
b SIMAP Laboratory, Université Grenoble Alpes, Grenoble, France
c Université de Bretagne Sud, IRDL, Centre de recherche, Rue ST Maudé, F-56100, Lorient, France
d CNRS, Université de Bordeaux, ICMCB, 87 avenue du Dr. A. Schweitzer, F-33608, Pessac, France

Keywords: Resistance upset welding, ODS steel, nuclear fuel cladding, microstructure, nano-precipitates, EBSD, SAXS.

Abstract
Development and characterization of clad-to-plug resistance upset welds is presented for two oxide dispersion strengthened steels candidates for sodium-cooled fast reactors fuel cladding: 9Cr ferrito-martensitic steel and 14Cr ferritic steel. A comparative approach is adopted regarding these two materials implying weldability studies and weld mechanical strength tests. A special attention is paid on welding metallurgical effects on the specific microstructure of these materials. Among others, some major grain property modifications by dynamic recrystallization and a slight modification of precipitate sizes and volume fraction are found and discussed.

1. INTRODUCTION

Ferritic and martensitic Oxide Dispersion Strengthened (ODS) steels are considered as candidate materials for the development of fuel cladding for sodium-cooled fast reactors (SFR). In particular, their ferritic and martensitic structure make them resistant to irradiation swelling and their nano-oxide uniform distribution gives them a good creep and high-temperature resistance [1].
Fuel clads are welded at each extremity to end-plugs made of the same material. It is known that traditional fusion welding processes generally deteriorate ODS properties due to microstructure changes (grain size, modifications of the nano-oxide distribution…) [2-4]. Consequently, solid-state welding processes are preferred.
One of the welding processes developed for ODS steel fuel clad welding is resistance upset welding. In this process, the fuel clad is pressed against the end plug and a high current is applied during a few milliseconds. Joule heating at the plug-to-clad contact associated with a compressive mechanical load is sufficient to ensure a proper weld joint.
Several authors published studies on the development of resistance upset welding and associated weldability for this application [5-11]. These studies show encouraging results regarding welding procedure development and weld mechanical strength. For example, Seki et al. [5] developed plug-to-clad welds on a 9 % chromium ODS steel able to resist to tensile, internal pressure burst and creep rupture tests, the failure occurring in the clad out of the welded zone. The plug-to-clad resistance weldability results are difficult to transpose from one study to another. They are indeed highly dependent on, among others, welding parameters, welding geometrical configuration (welded pieces and welding electrodes) and initial plug-to-clad contact geometry, data rarely fully given by the authors. Unlike welding procedure development studies, metallurgical weldability studies, i.e. the effect of resistance upset welding on ODS steel microstructure, are scarce. Only Corpace et al. [11] have shown that the level of deformations and temperatures reached during resistance upset welding of PM2000 ODS steel (20% chromium), trigger a dynamic recrystallization phenomenon in the welded area which is also usually combined with a modification of the nano-oxide dispersion.
On the contrary, many authors have studied metallurgical effects of solid-state Friction Stir Welding (FSW) on ODS steels. These studies mainly concern ferritic ODS steels in plate configurations. Major effects on microstructure are found which imply dynamic recrystallization in the stirred zones. Among

others, the grains get smaller than in base metal for large grain grades (i.e. initial sizes > 100 µm) [12] and larger than in base metal for small grain grades (i.e. initial around 1 µm) [13-16]. In literature, there are two major trends for the evolution of nano-oxides. When a welding effect is observed in the stirred zone, an increase of their size [8] or a decrease of the density of nanometer-size precipitates via agglomeration and coalescence mechanisms [12] [17-18] is reported. Nevertheless, some other articles do not notice any major effect on precipitates [14][19-20].
The quantitative characterization of nano-oxides is classically performed using small-angle scattering methods, which are particularly relevant to determine the size and fraction of extremely small particles (from 0.5 to 10 nm typically) in complex microstructures comprising small grains and possibly high dislocation densities. Although most studies have been made using neutrons (SANS) [21-23], an interesting alternative is the use of X-rays (SAXS) which has been coupled to SANS measurements [24] or used separately [25-26]. SAXS has the advantage, when compared to SANS, to permit in-situ measurements [27], and most importantly to make it possible to carry out measurements with a much higher spatial resolution when performed with a synchrotron beam (typically 200 µm as compared to several mm for SANS). This improved spatial resolution is a key advantage when mapping a heterogeneous microstructure such as encountered in a weld.

In this study, the development of plug-to-clad resistance upset welds and the assessment of welding effects on ODS steel grains and precipitates are reported. Two ODS steel grades, belonging to two different families, are compared: 14 wt% chromium ferritic steel (14Cr) and 9 wt% chromium ferrito-martensitic steel (9Cr).

2. MATERIALS AND METHODS

2.1 Materials

ODS steels are manufactured by powder metallurgy and mechanical alloying so as to obtain a fine homogeneous dispersion of nano-oxides within the matrix. The powder is then compacted and hot extruded to obtain a raw bar. Usually, the cladding tube is cold-worked afterwards but in our case, it was machined directly in the raw bar for material supply reasons. The end-plug was also machined in the same raw bar. The materials studied in this paper were hot extruded at 1100 °C after a preheating at 1100 °C for 1 hour. A heat treatment at 1050 °C for 1 hour was performed afterwards followed by a slow cooling (25 °C/h). The chemical composition of the two studied materials is Fe-14Cr-1W-0,3Ti-0,25Y_2O_3 and Fe-9Cr-1W-0,1C-0,3Ti-0,25Y_2O_3 (all in wt%). The two materials will be hereafter named respectively 14Cr and 9Cr, and were manufactured at CEA (SRMA/LTMeX laboratory). For both materials, solidus temperature T_S and liquidus temperature T_L are respectively about 1450 °C and 1500 °C.
14Cr is a ferritic steel whose matrix does not exhibit solid-state phase transformation between room temperature and the solidus.
9Cr is a ferritic-martensitic steel whose matrix exhibits solid-state phase transformations. The material used in this study was characterized by Toualbi [22]: A_{C1} = 850 °C, A_{C3} = 900 °C and A_{C4} = 1275 °C. The minimum cooling rate to obtain a fully martensitic structure was about 1 °C/s and its martensite starting temperature M_s is around 380 °C. Cladding tubes and end-plugs were in ferritic state when received.

14Cr was composed of two different grain populations: small equiaxed grains and large grains elongated toward the extrusion direction. The surface fraction of small and large grains was respectively 60 % and 40 %. The average size of small and large grains was respectively 1.1 ± 0.5 µm and 5.2 ± 2.7 µm. Both grain populations presented a α {hkl}<110> fiber texture, i.e. <110> grain direction is mainly parallel to the extrusion direction. This texture intensity was stronger for large grains than for small grains. For 9Cr, only one grain population, equiaxed with an average grain size of 4.6 ± 2.5 µm, was noticed. This material was almost not textured.
Precipitate size (including nano-oxide size) was assessed by SAXS and was described according to two populations: small and large precipitates. Figure 1 shows typical SAXS patterns for the 9Cr weld, along

with the modeled intensity with its two contributions. For 14Cr, the small and large precipitate populations presented an average radius of respectively 0.86 nm and 2.9 nm. The volume fraction of the small precipitates was about 2.5 times higher than that of the large precipitates. For 9Cr, the average radius of the small and large precipitate populations was respectively 1.3 nm and 3.7 nm. The volume fraction of the small precipitates was about 2 times higher than that of the large precipitates.

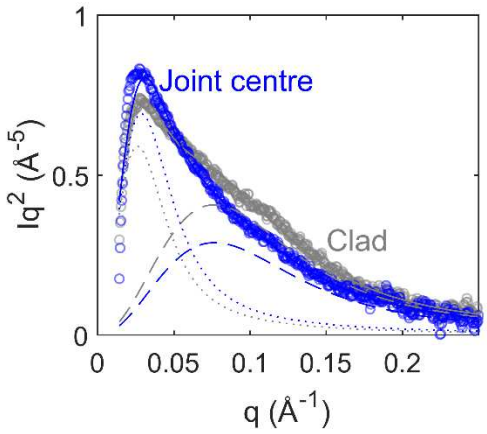

Figure 1 – Typical SAXS patterns of the clad zone as well as the joint center zone, represented as Iq^2 vs q (Kratky plot) for the 9Cr weld. Circles are the experimental data and solid lines are the modeled intensity, which sums two contributions of smaller and larger precipitates (dashed and dotted lines).

2.2 Welding operation and pieces geometry main features

The clad and the end-plug have an outside diameter between 9 and 11 mm and the clad has a thickness of 0.5 mm. The TECHNAX medium frequency welding device used (part of CEA's platform "ALTEA", Figure 2a) was presented in detail by Le Gloannec [28]. This welding device is instrumented and allows recording the welding parameters (voltage, current, force and welding time) and the end-plug displacement during the welding process.

During welding, clad and end-plug are both clamped into copper alloy electrodes. Those electrodes are tightened into jaws through which the electrical current passes. A pneumatic jack pushes the end-plug on the clad (fixed carriage). Heating is ensured by a 1 kHz alternative current which is rectified and smoothed. The current intensity is ramped-up to a maximum value, held constant for a given dwell time and then ramped-down (Figure 2b). The weld starts forming once high temperatures are reached around the plug-to-clad contact. Then, under the compressive force, the plug and clad are compressed one inside the other.

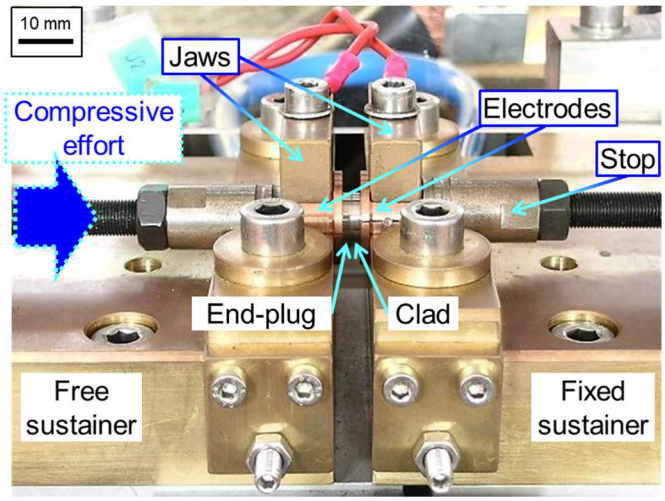

a)

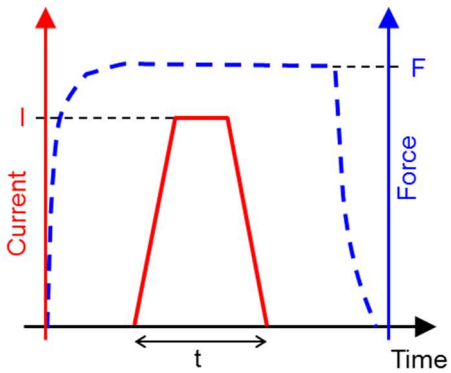

b)

Figure 2 – Central view of the resistance upset welding device part of CEA's platform "ALTEA" *(a), and representation of the welding parameters evolution with time (b).*

The main welding parameters, optimized to create welds without defects (i.e. without lack of bonding, melting and cracks), are current intensity I, total welding time t and compressive force value F (Figure 2b). The optimized parameter values are between 10 and 20 kA for I, 10 and 80 ms for t, and 2000 and 5000 N for F. These values are similar for 14Cr and 9Cr steels. Welding and geometrical parameter values were chosen to produce welds without melting, unlike what has been reported by De Burbure [7] where the melted material is ejected out of the weld by the compressive force. In our case, no machining was needed after welding because no external burr is present.

2.3 Weld characterizations

Welded assemblies were first qualitatively tested to perform weld defects detection via conventional helium leakage tests (detection threshold of 10^{-4} mbar.L.s^{-1}) and micrographic observations (mirror polishing and chemical etching with Vilella's reactant) of three circumferential cuts locations per weld (0°, 180° and 270°). Tests were performed for each material. The main defects investigated were: lack of bonding (especially at low welding energy), local fusion (especially at high welding energy), and cracks or crack initiations.

Additional qualitative weld quality tests were performed via two different tests at room temperature, by mechanical strength assessment of the welded assembly: (a) burst tests, performed on ALTEA platform, which stresses the welded assembly by internal pressure (hoop stresses in the clad, 3.10^7 Pa/min) and (b) axial tensile tests (5.10^{-4} s^{-1}) on specific samples made of a clad welded with a threaded plug at both extremities (i.e. each sample contains two similar welds). Those two tests present different stress directions (in the clad, hoop direction in burst test and axial direction in tensile test) which makes them complementary with regards to crack propagation. In order to validate the tests, assemblies should exhibit a failure outside of the welded zone (i.e. in the clad) and failure pressure or stress equivalent or higher than the failure values of the clad alone. To assess what we will call a 'safety margin' of the welding parameters versus these tests, we also performed these tests on additional assemblies that were welded using sensitively smaller welding intensity values than the optimized one (while keeping the other parameters constant) in order to make the failure occur in the weld.

2.4 Material characterizations

Electron Back Scatter Diffraction (EBSD-SEM) characterizations were performed on a SUPRA 55VP Scanning Electron Microscope (SEM) from Zeiss. Data processing was made via OIM (Orientation Imaging Microscopy) software from TSL. The characterized welds were basically constituted of a clad-plug joint plane potentially surrounded by a thermo-mechanically affected zone (TMAZ) and/or a heat affected zone (HAZ) which was also surrounded by the base material (BM). Small dimensions of the weld have made the map localization difficult especially when grains were of a few µm. Consequently, large maps were made in the base metal (100 x 60 µm²) far from the weld and across the weld (700 x 60 µm²) perpendicular to the clad axis. For all, a step of 0.1 µm was used. Grain boundaries were defined by a misorientation greater than or equal to 10 °. In IPF (Inverse Pole Figure) maps, the horizontal axis was the extrusion direction. The clad axis (ED) and the radial direction (RD) on pole figures, corresponded respectively to the horizontal and the vertical direction of IPF maps. Grain sizes were assessed by the equivalent circle method.

Small Angle X-ray Scattering (SAXS) measurements were performed at the European Synchrotron Radiation Facility (ESRF) on the BM02-D2AM beamline to characterize the evolution of size and the volume fraction of precipitates (including nano-oxides). Since the measurement of the volume fraction of precipitates in absolute values depends on the chemistry of these particles, which may experience some deviation from the classically considered $Y_2Ti_2O_7$ composition, we adopted a relative approach assessing the effect of welding on the integrated intensity which is proportional to volume fraction for a given chemistry of the precipitates [29]. Measurements were performed on foils of thicknesses

between 70 and 100 µm. The energy was 16.738 keV with a sample-to-detector distance of about 1.3 m. This allowed to cover the range of scattering vectors from 0.15 nm^{-1} to 3.3 nm^{-1}. The scattering vector is given by $q = \frac{4\pi\sin(\theta)}{\lambda}$ with λ the wavelength and θ the half scattering angle [30]. A zone of 800 µm * 700 µm centered on the weld was scanned. The position of the analyzed zone was estimated by mapping the sample thickness by transmission measurements, since it is smaller on the clad edges. The scan step was 100 µm and for each SAXS measurement, the size of the analyzed zone (i.e. the beam size) was about 300 µm * 200 µm (respectively in the clad axis and radial directions).

Wavelength-dispersive spectroscopy (WDS) was used to assess at µm scale welding effects on chemical elements such as Yttrium and Titanium which compose the nano-oxides. Maps were acquired via a CAMECA SX100 probe with a voltage of 20 kV. The analyzed volume of each measured point being about 1 μm^3, these WDS maps aimed at visualizing potential nano-oxide cluster formation or major elements distribution changes, as mentioned by Corpace [11]. Scan steps were 1 µm far from the weld and 0.2 µm inside the weld.

3. Results and discussions

3.1 Weld quality and micro-hardness

Both 14Cr and 9Cr showed good leak tightness during helium leak tests.

No defect was detected on the micrographs for 14Cr welds: a good compactness is obtained and no local fusion occurs. As illustrated in Figure 3, the initial clad-to-plug contact is not visible anymore. Its trace is indicated with a light blue dotted curve named in the following "joint plane trace". Almost no defect is encountered on 9Cr welds, based on micrographs observations. Twice (out of 20 welds), cracks (about 50 µm long) were observed located at one extremity of the joint plane trace. This susceptibility to cracks has already been noticed by Seki et al. [5] for 9Cr resistance welding, who developed a non-destructive examination process to detect them.

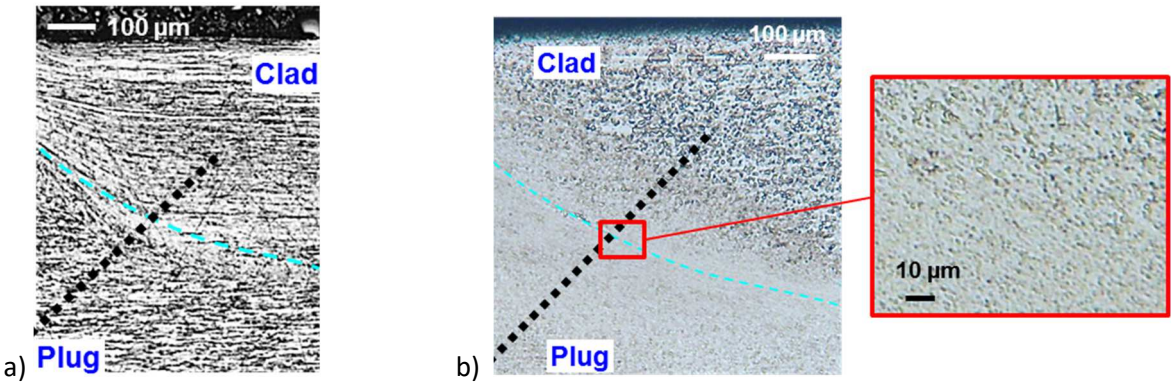

Figure 3 – Weld micrographs: 14Cr (a) and 9Cr (b). The light blue dotted curve represents the approximate joint plane trace and the black dotted line represents the micro-hardness line-scans illustrated in Figure 5.

For both 14Cr and 9Cr, welds were always stronger than the clad in burst tests. The failure occurred in the clad outside of the welded zone (Figure 4a for 9Cr). To generate a failure in the weld, the welding intensity had to be decreased by more than 27 % from its optimized value for both materials. The so-called safety margin regarding this test, is thus very large.

For tensile tests, welds were also always stronger than the clad whatever the material. Failure occured around the middle of the clad length for the end-plug/clad/end-plug welded sample (figure 4b for 14Cr). However, in comparison with burst tests, tensile tests showed a smaller safety margin. To generate a failure in the weld, the welding intensity had to be decreased by more than 15 % for 14Cr and 9 % for 9Cr from their optimized values.

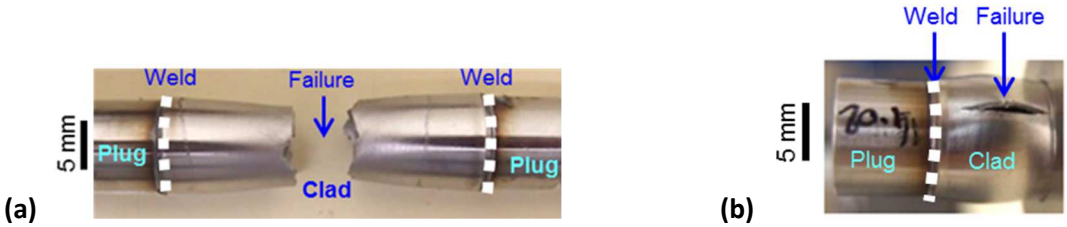

Figure 4 – Image of a 14Cr end-plug/clad/end-plug welded sample after a tensile test (a), and image of a 9Cr end-plug/clad welded assembly after a burst test (b). The welds are located under the white dashed lines.

Vickers micro-hardness line-scans were performed across the weld for each material and weld parameters, from the end-plug base metal to the clad base metal. The line-scan angle was 45° versus the clad axis, which made it almost perpendicular to the trace of the joint plane (Figure 3). $HV_{0.1}$ (100 g) micro-hardness was measured with a 0.05 mm step.

Micro-hardness scans on 14Cr welds indicate no hardness value change in the weld with respect to base metal (Figure 5). A constant value of 430 ± 17 $HV_{0.1}$ was found in the clad far from the weld up to the plug far from the weld. For 9Cr, results showed a large increase of micro-hardness values in the welded zone with respect to BM (Figure 5). Micro-hardness value varied from 290 ± 20 $HV_{0.1}$ in BM up to 540 ± 16 $HV_{0.1}$. Higher hardness values are localized on a plateau of about 1 mm large.

This increase of hardness values could be explained by the presence of martensite. A heat treatment at 760 °C for 45 minutes allowed us to decrease the hardness of this 1mm wide area down to the hardness of the BM (300 ± 29 $HV_{0.1}$), as already mentioned by Seki et al. [5]. This kind of heat treatment is classically performed on traditional martensitic steels with 9 % chromium such as X10CrMoVNb9-1 [31], to obtain tempered martensite from quenched martensite. The microstructural analyses in the following are made on samples without this additional heat treatment.

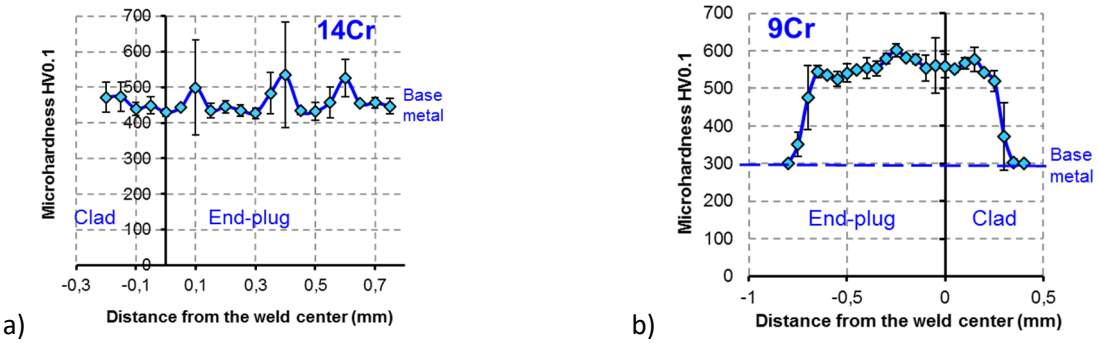

Figure 5 – Micro-hardness $HV_{0.1}$ evolutions across the weld zone: for 14Cr (a) and 9Cr (b).

3.2 Welding effects on grain microstructure and nano-oxides

To understand the results obtained in the previous section and also because reduction of grain size due to dynamic recrystallization and modification of the nano dispersed oxides were already observed in the welded zone [11] during resistance upset welding of fuel claddings, microstructural analyses were conducted at different scales in the area of the weld directly after welding.

3.2.1 Microstructure

The description of the welded area depends on the ODS steel. However, for both steels, three different homogeneous zones in terms of grain size and texture were present.
Figure 6 summarizes the EBSD results obtained for 14Cr welds. Even if the $HV_{0.1}$ profile across the weld is almost uniform, three different zones were identified: 1) base metal (BM), 2) a central band around the joint plane trace of about 100 µm wide also called central Thermo-Mechanically Affected Zone or central TMAZ and 3) a transition zone of a few tens of µm between the BM and TMAZ also called transition TMAZ. The BM zone exhibits two grain populations: large elongated grains and small equiaxed grains (respectively 5.2 ± 2.7 µm and 1.1 ± 0.5 µm), similar to the as-received 14Cr steel. The central TMAZ band showed only small grains of an average size of 1.2 ± 0.8 µm. These grains were quasi equiaxed, meaning that the large elongated grains from BM have disappeared. The transition TMAZ showed intermediate microstructure with elongated grains but a less pronounced α-fiber texture (cf. {110} pole figures in Figure 6). The maximum texture intensity was 3.7 for the transition TMAZ, in comparison with 6.8 for BM. In the central TMAZ, texture was changed and similar to the shear texture observed by Karch [32] after a shear stress on the same ODS steel grade, by Chen [19] and Wang [12] on a 20 % chromium ferritic ODS FSW weld and by Baczynski [33] on non ODS steels.
Figure 7 shows EBSD maps of 9Cr welds (without subsequent heat treatment). As for 14Cr, three different zones are present: 1) BM, 2) a central band around the joint plane trace of about 100 µm wide called TMAZ and 3) a zone around the central band of about 450 µm on the plug side and 150 µm on the clad side, called HAZ. The TMAZ exhibits equiaxed grains with a smaller average size than for the BM: 1.5 ± 0.9 µm in comparison with 4.6 ± 2.5 µm for BM. The HAZ shows a specific microstructure made of grains with an average size of 2.9 ± 2 µm and presenting a lot of sub-structures and small grains (about or less than 1 µm) without any particular morphology. Regarding {110} pole figures (Figure 7), as observed in the central TMAZ of 14Cr, for TMAZ a shear texture was found. In the HAZ, the α-fiber texture is attenuated but more similar to the BM texture.
Both 14Cr and 9Cr welds are thus characterized by a central band with a refined grain structure. These bands have similar morphological and crystallographic textures (small equiaxed grains and a shear texture).

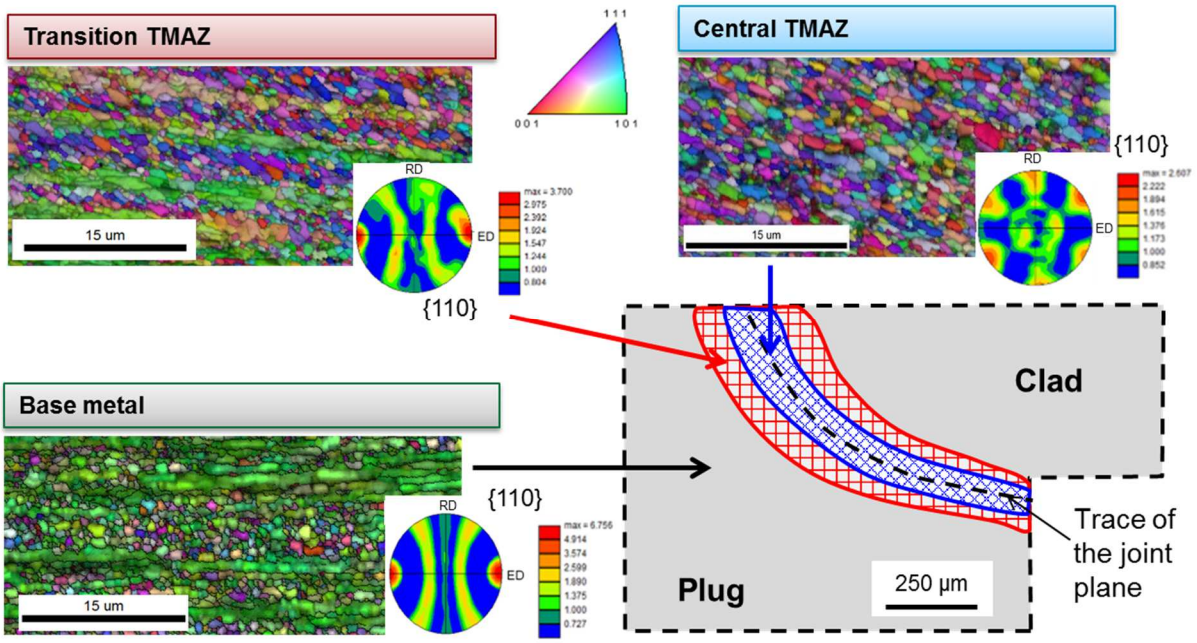

Figure 6 – IPF maps and {110} pole figures: illustration of the three different zones in terms of grain properties on a 14Cr weld schematic; Base material (BM), Transition Thermo-Mechanically Affected Zone (Transition TMAZ) and central Thermo-Mechanically Affected Zone (Central TMAZ).

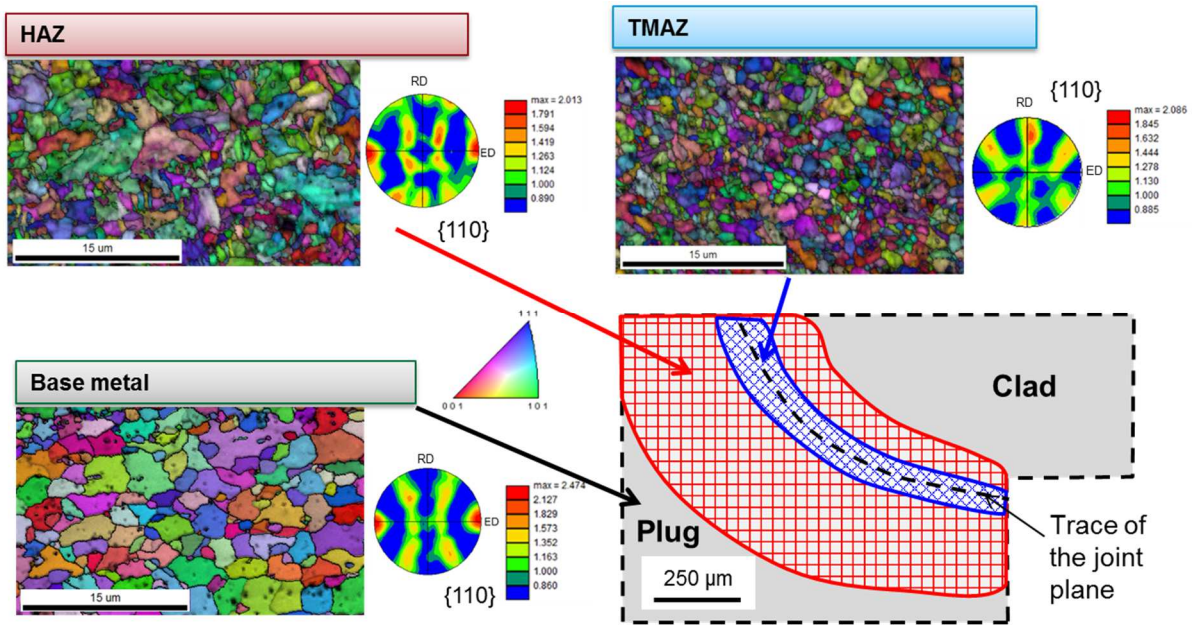

Figure 7 - IPF maps and {110} pole figures: illustration of the three different zones in terms of grain properties on a 9Cr weld schematic (before heat treatment); Base material (BM), Thermo-Mechanically Affected Zone (TMAZ) and Heat Affected Zone (HAZ).

In order to get more insight of the phenomena occurring during welding, numerical simulations of this welding operation were performed using a model developed by Le Gloannec [28] for the resistance upset welding of X10CrMoVNb9-1 ODS steels. The geometry and boundary conditions of the original model were modified to fit the experimental conditions of our configuration. Temperatures and plastic strains evolution during welding were assessed and compared to experimental outputs.
The highest strains predicted by these simulations (plastic cumulative strains up to 5) are concentrated in a zone corresponding to the TMAZ previously identified. These strains are mainly dominated by shearing parallel to the joint place trace. The maximum temperature estimated in this zone is close to 1350 °C.
Simulations show that the mechanical stresses in the transition zone surrounding the central TMAZ is different whether we consider 14Cr or 9Cr. For 14Cr, the transition zone is also a TMAZ but with lower strains and temperatures compared to the central TMAZ while for 9Cr, strains are almost zero in this area, justifying the name HAZ for 9Cr.
The equiaxed grain refinement occurring in both TMAZ can be attributed to dynamic recrystallization. The transformation from a α-fiber texture to a shear texture is attributed to the intense shear strains that take place in this zone. The mechanisms (continuous or discontinuous) associated with this dynamic recrystallization cannot be identified based on these results. For ODS ferritic steel plates at high temperature and high plastic strains mainly in shearing during FSW [26][27], dynamic recrystallization and shear texture were already observed [12, 19] without any more detailed information on recrystallization mechanism.

For 9Cr, martensite might be present in the HAZ, but as shown by Hary [36] and Zilnyk [37], it is difficult to identify lath or plate-shaped structures on martensitic ODS steels by EBSD. Only reduction of the image quality maps when compared with those of BM and TMAZ could attest its formation. In the HAZ, maximum calculated temperature ranges from 850 °C to 1250 °C. Heating and cooling rates are assessed respectively to be of the order of $+10^5$ °C/s and -10^3 °C/s. This welding cooling rate exceeds by several orders of magnitude the critical cooling rate of 1 °C/s to obtain martensite. Moreover, the

maximal temperature reached is lower than the appearance temperature of delta ferrite at equilibrium (1275 °C). HAZ microstructures were observed to be uniform even at the vicinity of the BM where the maximum reached temperature is around 850 °C. The microstructure of the 9Cr has not been characterized for these rates in the literature. We performed dilatometry tests using a Gleeble 3500 machine, on 9Cr rod samples with heating and cooling rates of respectively $+10^3$ °C/s and $-2*10^2$ °C/s. These are the highest rates possible with this sample geometry and the system configuration used. These tests confirmed the creation of martensite. Moreover, by comparing micro-hardness profiles and the EBSD results, we noticed that the high hardness plateau size was similar to the cumulative size of HAZ and TMAZ. Given these considerations, the presence of martensite seems highly probable in the 9Cr HAZ. In the TMAZ, the presence of very high temperatures allows the possibility to create delta ferrite even if martensite presence is also possible.

3.2.2 Nano-oxides

For 9Cr (Figure 8), WDS maps showed no significant modification of yttrium and titanium distribution in the welded area at µm scale, meaning that there was no macroscopic change in nano-oxides distribution [11]. The Yttrium uniform distribution as well as the Titanium enriched dots, also present in the BM, are still visible in HAZ and TMAZ without any modification. Similar results are obtained for 14Cr.

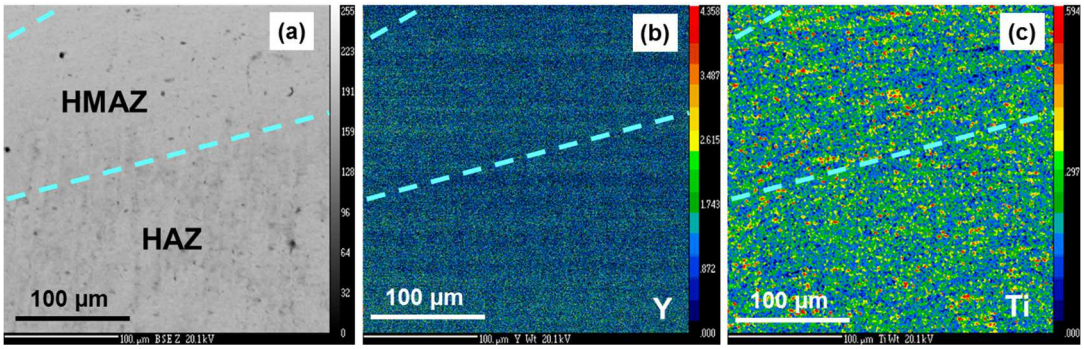

Figure 8 – Illustrations of chemical element distributions obtained by WDS for 9Cr welds: (a) backscattered electron image, (b) Yttrium map and (c) Titanium map (increasing concentration from blue to red color).

SAXS measurements analyses were used to assess any visible effect of welding on the size distribution of precipitates (including nano-oxides). Results presented in Figure 9 for 14Cr and Figure 10 for 9Cr, show the evolution of the precipitates (volume weighted) average radius and (total) integrated intensity (Figure 9a) as a function of the distance to the joint plane along the dark arrow represented on the scheme (Figure 9b and 10b) of the welded area in order to localize the analyses. Figures 9c-e and 10c-e are SAXS maps of the evolution of the radius and the integrated intensity for small and large precipitates separately.

Regarding 14Cr (Figure 9), far from the weld the average size of the precipitates is about 0.9 nm and their average integrated intensity about 0.15 $Å^{-6}$. The integrated intensity (i.e. the volume fraction) does not evolve much close to the joint plane, but the average size slightly increases. Along with the visual information given by the separate mapping of the small and large populations, it appears that the volume fraction remains essentially constant while there is a significant coarsening of some of the precipitates.

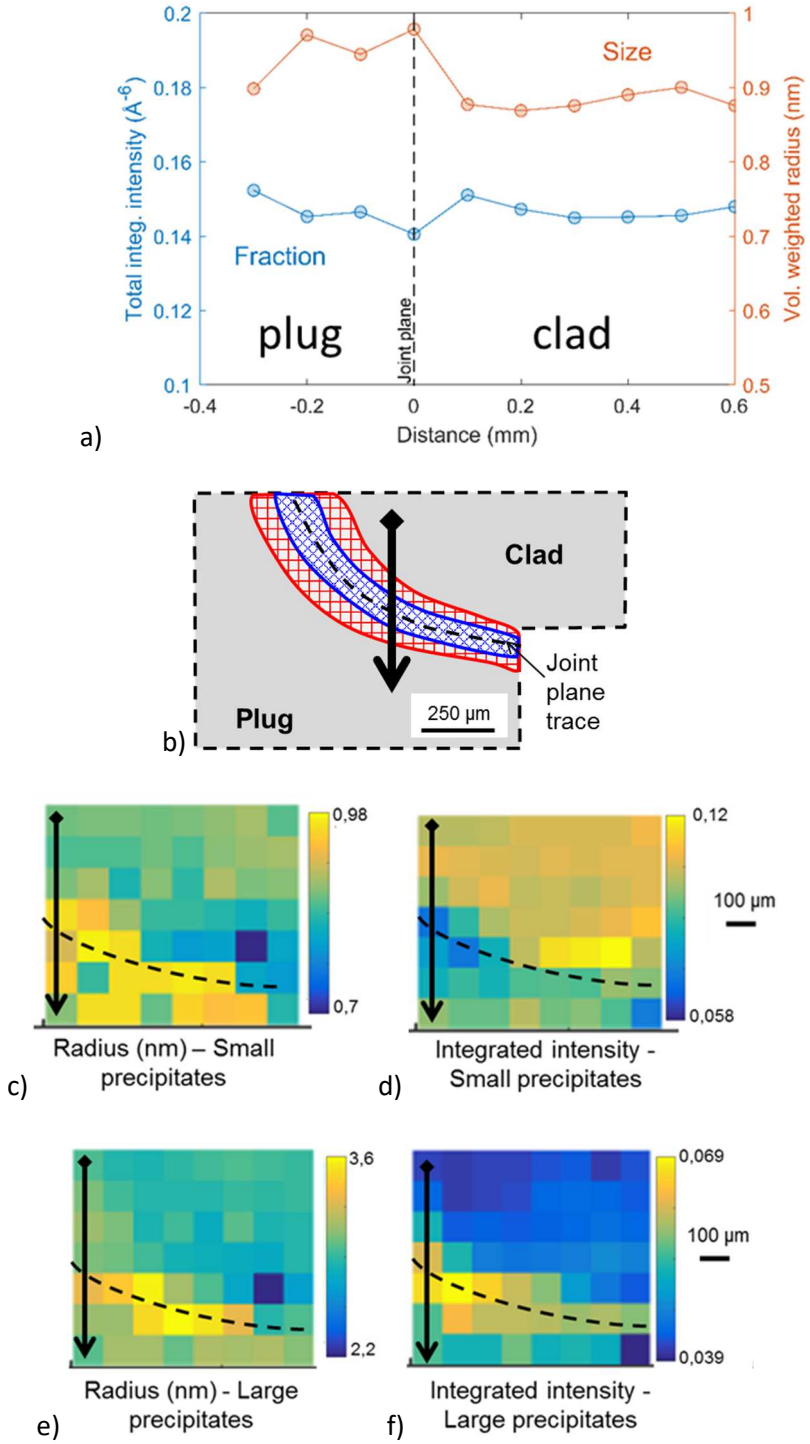

Figure 9 – 14Cr welded area: a) Precipitate radius (nm) and integrated intensity (Å^{-6}) evolution as a function of the distance to the joint plane along the dark arrow represented on the schema (b). SAXS maps for the small (c)-(d) and large (e)-(f) precipitate populations. More explanations can be found in sections 2.1 and 2.4.

For 9Cr (Figure 10), the average size of small precipitates far from the weld is 1.3 nm and the total integrated intensity about 0.1 Å^{-6}, 50% lower than that of the 14Cr. Similarly to the case of the 14Cr, the total integrated intensity does not evolve much, with a possible slight decrease close to the trace of the joint plane. This effect can be due to the larger precipitates becoming too large to be observed by our setup. The average size does show a slight increase close to the joint, which is likely to be underestimated if larger precipitates are being ignored by the measurements.

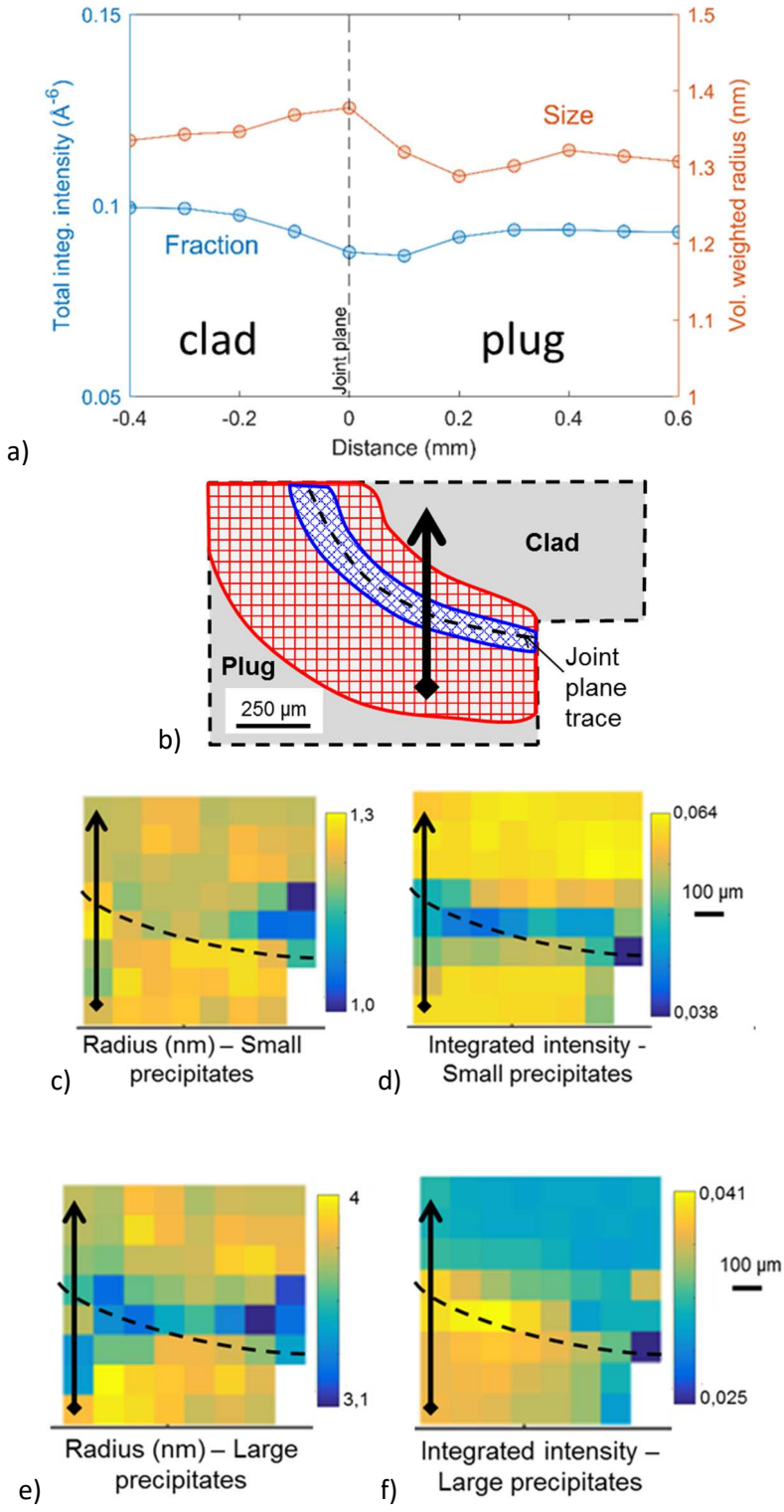

Figure 10 – 9Cr welded area: a) Precipitate radius (nm) and b) integrated intensity ($Å^{-6}$) evolution as a function of the distance to the joint plane along the dark arrow represented on the schema (c). SAXS cartographies for the small (d) and large (e) precipitate populations. More explanations can be found in sections 2.1 and 2.4.

The size of the precipitate modification zones is coherent with the TMAZs sizes identified in section 3.2.1 (about 100 to 200 µm) where the modifications of grain microstructures are the most visible.

The conclusions drawn from the SAXS measurements (slight increase of precipitates radii with an essentially constant total volume fraction) remain semi-quantitative because of their limited spatial resolution. Indeed, the analyzed zone size (equal to the X-ray beam size) is about 300 µm x 200 µm. This zone is larger than the TMAZ width (about 100 µm for 9Cr and 100 to 200 µm for 14Cr). Thus the measured values at each position are a spatial convolution of the actual microstructure evolution. It can be expected that the current measurements underestimate the microstructure modifications actually occurring in the different zones because of this averaging with some unaffected material. SAXS measurements with a smaller beam size or made on specimens with larger affected zones would be required to make more definitive estimates on nano-oxide modifications.
Mathon et al. [38] observed by SANS FSW welds of an ODS ferritic steel with dimensions more adapted to the experiment's spatial resolution, and showed a precipitate size increase towards the center of the weld. However, some precipitates became too big at the weld center to be characterized with their set-up. This result is consistent with our conclusions obtained with a different welding process subjected to similar local thermo-mechanical stresses (high temperatures and high plastic strains mainly in shearing mode).
The increase of the precipitates size in the weld also combined with a reduction of grain size, could explain for 14Cr the stability of the HV values with the hypothesis that a print has been done in the thin central and transition TMAZ areas.

4. CONCLUSION

We have presented the development and characterization of clad-to-end-plug resistance upset welds for two candidate materials for fuel cladding: a 14Cr ODS ferritic steel and a 9Cr ODS ferritic-martensitic steel. A focus was made on the effects of welding on the specific microstructure of these materials, both at the scale of the grain size and at the scale of the nano-oxides. The following points are highlighted.

1. Investigations of the effect of welding on grain morphology showed the presence in both materials of a 100 µm wide central band along the trace of the joint plane, which differs from the base metal. This zone is a TMAZ whose grains have been generated by dynamic recrystallization leading to equiaxed grain refinement and a shear texture. Around this zone, a large HAZ probably made of martensite is found in the 9Cr material, whereas a narrow transition TMAZ is found for 14Cr.
2. A fine nano-oxide distribution is still present in all weld zones. Nevertheless, some changes in the characteristics of this distribution (size and volume fraction) have been characterized by synchrotron SAXS mapping. Close to the joint plane trace, i.e. in the TMAZs, the total oxide volume fraction does not evolve much, but their size increases, as illustrated by the transfer of some of the smallest oxides (around 1 nm in radius) to a population with larger size (around 3-4 nm in radius). This evolution is present in both materials.
3. For both materials, the plug-to-clad welds developed present a very good helium leak tightness, a very good resistance to burst tests at room temperature and a good resistance to tensile tests at room temperature. Unlike for 9Cr, no susceptibility to welding crack initiations was found for 14Cr (based on micrographs observations) and no post welding heat treatment was needed.

This work on weld characteristics after welding operation will be followed in the future by a similar work closer to reactor conditions (such as high temperature behavior, thermal and irradiation aging effects). An irradiation campaign of the welds is already in progress in BOR60 reactor.

Acknowledgment
The authors thank Michel Lahaye (PLACAMAT, Bordeaux, France) for the WDS analyses. The staff at BM02-D2AM beamline of ESRF is thanked for technical support.

References

[1] P. Dubuisson, Y. De Carlan, V. Garat, M. Blat, ''ODS ferritic/martensitic alloys for sodium fast reactor fuel pin cladding'', J. Nucl. Mater. 428 (2012) 6–12.
[2] M.G. McKimpson and D. Odonnell, "Joining ODS materials for high-temperature applications", JOM 46 7 (1994) 49-51.
[3] G. H. Gessinger, "Joining techniques for P/M superalloys", in Powder Metallurgy of Superalloys, Baden, Switzerland: Buttefworth & Co. (1984) 295–327.
[4] T. Kelly, "Welding of mechanically alloyed ODS materials", in Trends in welding research in the United States, S. A. David (1981) 471–485.
[4] M. Seki, K. Hirako, S. Kono, Y. Kihara, T. Kaito, and S. Ukai, "Pressurized resistance welding technology development in 9Cr-ODS martensitic steels", J. Nucl. Mater. 329–333 (2004) 1534–1538.
[6] S. De Burbure, "Resistance butt welding of dispersion-hardened ferritic steels", in Advances in Welding Processes 3rd International conference (1975).
[7] S. De Burbure, "Resistance welding of pressurized capsules for in-pile creep experiments", Weld. J. 57 11, (1978) 23–30.
[8] L. Zirker, N. D. Jerred, I. Charit, J. I. Cole, "History of Resistance Welding Oxide Dispersion Strengthened Cladding and other High Temperature Materials at Center for Advanced Energy Studies", Idaho National Laboratory, INL/EXT-12-2528 (2012).
[9] L. R. Zirker, J. H. Bottcher, S. Shikakura, C. L. Tsai, and M. L. Hamilton, "Fabrication of oxide dispersion strengthened ferritic clad fuel pins", Argone National Laboratory, ANL/CP--72041 (1991).
[10] N. Jerred, L. Zirker, B. Jacques, T. Bradshaw, I. Charit, J. Cole, M. Frary, D. Butt, M. Meyer, and K. L. Murty, "Pressure Resistance Welding of High Temperature Metallic Materials", Idaho National Laboratory, INL/CON--10-19185 (2010).
[11] F. Corpace, A. Monnier, J. Grall, J-P. Manaud, M. Lahaye, A. Poulon-Quintin, "Resistance Upset Welding of ODS Steel Fuel Claddings – Evaluation of a Process Parameter Range Based on Metallurgical Observations", Metals 7 9 (2017) 333.
[12] J. Wang, W. Yuan, R. S. Mishra, and I. Charit, "Microstructural and mechanical properties of friction stir welded oxide dispersion strengthened alloy", J. Nucl. Mater. 432 (2013) 274–280.
[13] K. Dawson, S. Cater, G. J. Tatlock, and C. Stanhope, "Friction stir welding of PM2000 ODS alloy", Mater. Sci. and Tech. 30 13b (2014) 1685–1690.
[14] S. Noh, R. Kasada, A. Kimura, S. H. C. Park, and S. Hirano, "Microstructure and mechanical properties of friction stir processed ODS ferritic steels", J. Nucl. Mater. 417 1–3 (2011) 245–248.
[15] B. W. Baker and L. N. Brewer, "Joining of Oxide Dispersion Strengthened Steels for Advanced Reactors", JOM, 66 12 (2014) 2442–2457.
[16] B. W. Baker, T. R. McNelley, and L. N. Brewer, "Grain size and particle dispersion effects on the tensile behavior of friction stir welded MA956 oxide dispersion strengthened steel from low to elevated temperature", Mater. Sci. Eng. A 589 (2014) 217–227.
[17] C. Y. Kang, T. H. North, and D. D. Perovic, "Microstructural Features of Friction Welded MA 956 Superalloy Material", Metall. Mater. Trans. A 27A (1996) 4019–4029.
[18] N. D. Jerred, I. Charit, L. R. Zirker, J. I. Cole, Pressure resistance welding of MA-957 to HT-9 for advanced reactor applications, Journal of Nuclear Materials, 508 (2018) 265-277.
[19] C.-L. Chen, G. J. Tatlock, and a. R. Jones, "Microstructural evolution in friction stir welding of nanostructured ODS alloys", J. Alloys Compd. 504 (2010) S460–S466.
[20] C.-L. Chen, P. Wang, and G. J. Tatlock, "Phase transformations in yttrium–aluminium oxides in friction stir welded and recrystallised PM2000 alloys", Mater. High Temp. 26 3 (2009) 299–303.
[21] M. H. Mathon, M. Perrut, S. Y. Zhonga, Y. de Carlan , ''Small angle neutron scattering study of martensitic/ferritic ODS alloys'', J. Nucl. Mater. 428 1–3 (2012) 147-153.
[22] L. Toualbi, C. Cayron, P. Olier, J. Malaplate, M. Praud, M. H. Mathon, D. Bossu, E. Rouesne, a. Montani, R. Logé, and Y. De Carlan, "Assessment of a new fabrication route for Fe-9Cr-1W ODS cladding tubes", J. Nucl. Mater. 1–3 (2012) 47–53.
[23] G. R. Odette, M. J. Alinger, B. D. Wirth, ''Recent Developments in Irradiation-Resistant Steels'', Annu Rev Mater Res 38 (2008) 471–503.
[24] M. Ohnuma, J. Suzuki, S. Ohtsuka, S.W. Kim, T. Kaito, M. Inoue, and H. Kitazawa, ''A new method for the quantitative analysis of the scale and composition of nanosized oxide in 9Cr-ODS steel'', Acta Mater., 57 (2009) 5571– 81.
[25] M. Dadé, J. Malaplate, J. Garnier, F. De Geuser, N. Lochet, et al., ''Influence of consolidation methods on the recrystallization kinetics of a Fe–14Cr based ODS steel'', Journal of Nuclear Materials, 472 (2016) 143-152.
[26] M. Dadé, J. Malaplate, J. Garnier, Frédéric De Geuser, F. Barcelo, et al., "Influence of microstructural parameters on the mechanical properties of oxide dispersion strengthened Fe-14Cr steels", Acta Materialia, 127 (2017) 165 – 177.
[27] A. Deschamps, F. De Geuser, J. Malaplate, D. Sornin, "When do oxide precipitates form during consolidation of oxide dispersion strengthened steels?", Journal of Nuclear Materials, 482 (2016) 83-87.
[28] B. Le Gloannec, O. Doyen, C. Pouvreau, A. Doghri, A. Poulon-Quintin, Numerical simulation of resistance upset welding in rod to tube configuration with contact resistance determination, Journal of Materials Processing Technology 238 (2016) 409–422.
[29] F. De Geuser, A. Deschamps, Precipitate characterisation in metallic systems by small-angle X-ray or neutron scattering, C. R. Physique. 13 (2012) 246–256.
[30] F. De Geuser, A. Deschamps, "Precipitate characterization in metallic systems by small-angle X-ray or neutron scattering", C. R. Phys. 13 (2012) 246-256.
[31] R. L. Klueh and D. R. Harries, "High-Chromium Ferritic and Martensitic Steels for Nuclear Applications", ASTM, MONO3, (2001).

[32] A. Karch, “Étude des évolutions microstructurales lors de la transformation à chaud d’aciers ferritiques renforcés par dispersion d’oxydes”, PhD thesis, Ecole nationale supérieure des Mines de Paris, France (2014).
[33] J. Baczynski and J. J. Jonas, “Texture development during the torsion testing of alpha-iron and two if steels”, Acta Mater. 44 11 (1996) 4273–4288.
[34] J. Cho, D. E. Boyce, and P. R. Dawson, “Modeling strain hardening and texture evolution in friction stir welding of stainless steel”, Mater. Sci. Eng. A 398 (2005) 146–163.
[35] J. Cho and P. R. Dawson, “Investigation on Texture Evolution during Friction Stir Welding of Stainless Steel”, Metall. Mater. Trans. A 37 (2006) 1147–1164.
[36] B. Hary, T. Guilbert, P. Wident, T. Baudin, R. Logé, and Y. De Carlan, “Investigation of the relationships between mechanical properties and microstructure in a Fe-9 % Cr ODS steel”, EPJ Nucl. Sci. Technol. 2 7 (2016).
[37] K. D. Zilnyk, V. B. Oliveira, H. R. Z. Sandim, A. Möslang, and D. Raabe, “Martensitic transformation in Eurofer-97 and ODS-Eurofer steels: A comparative study”, J. Nucl. Mater. 462 (2015) 360–367.
[38] M. H. Mathon, V. Klosek, Y. de Carlan, and L. Forest, “Study of PM2000 microstructure evolution following FSW process”, J. Nucl. Mater. 386–388 (2009) 475–478.